Croatian Society for Materials Protection

Metalurgija/Metallurgy

Vol. 66 No. 1 / 2027

Fabrication of MgO Transparent Ceramics by Spark Plasma Sintering

Li-li Guo [1,2], Xi Sun [1*], and Wei-na Han [1*]

https://doi.org/10.64486/m.66.1.4

1 Liaoning Provincial Key Laboratory of Energy Storage and Utilization, Yingkou Institute of Technology, Yingkou, 115014, China
2 School of Metallurgy, Northeastern University, Shenyang, 110819, China
* Correspondence: sunxi0524@163.com; hanweina2025@126.com

Type of the Paper: Article
Received: February 14, 2026
Accepted: May 10, 2026

Abstract: In this work, MgO transparent ceramics were fabricated via spark plasma sintering (SPS) with Y_2O_3 as a sintering aid. The effects of sintering temperature, holding time, and Y_2O_3 content on the densification, microstructure, and optical transmittance of the ceramics were systematically investigated. Results indicate that optimizing SPS process parameters combined with an appropriate Y_2O_3 addition remarkably enhances the performance of MgO ceramics. Specifically, when sintered at 1350 °C for 10 min with 1.5 wt % Y_2O_3 doping, the MgO ceramic achieves high relative density and a maximum in-line transmittance of 75.35 % (mid-infrared range). Mechanistically, based on XRD lattice parameter analysis and SEM microstructural observations, Y^{3+} ions (ionic radius: 0.89 Å) are inferred to dissolve into the MgO lattice (Mg^{2+} ionic radius: 0.72 Å), inducing lattice distortion that is favorable for densification and grain growth inhibition. Excess Y_2O_3 (beyond 1 wt %) tends to segregate at grain boundaries, exerting a grain refinement effect via the Zener pinning mechanism. This study provides an effective strategy for the low-temperature fabrication of high-transmittance MgO transparent ceramics, thereby laying a solid foundation for the development of infrared (IR) window materials.

Keywords: transparent MgO ceramics; spark plasma sintering (SPS); Y_2O_3 sintering aid; infrared window materials; densification; optical transmittance

1. Introduction

A growing interest in transparent ceramics for various optical components, laser materials, scintillators, and more is evident in recent years [1–4]. One of the promising materials for infrared (IR) window applications is magnesium oxide (MgO) due to its high melting point (~2800 °C), wide transmission range (300 nm to 6 μm) and excellent thermo-mechanical properties [5–7]. Optical transmittance is crucial for evaluating MgO's applicability in IR windows, as it directly reflects the material's internal density, grain uniformity, and defect state—key factors determining signal transmission efficiency in optical systems [8–10]. Compared with commonly used mid-IR window materials such as Al_2O_3, $MgAl_2O_4$, and AlON, MgO offers lower absorption and better resistance to thermal shock, making it a promising choice for next-generation IR windows [11–14]. Nevertheless, the fabrication of fully dense, highly transparent MgO remains a significant challenge, as conventional sintering often requires extremely high temperatures and tends to induce exaggerated grain growth.

Considerable efforts have been made to overcome these challenges using different densification techniques [15–16]. Pressureless sintering of nanocrystalline MgO powders has achieved high density but only limited transparency. Hot isostatic pressing (HIP) has produced MgO ceramics with relative densities above 99.9 % and

in-line transmittance up to ~65 % of single crystals in the visible–near IR range. Spark plasma sintering (SPS) offers rapid densification while retaining fine grains, yielding nanocrystalline MgO with (40–60) % of single-crystal transmittance at selected wavelengths [17]. Chaim et al. [18] reported the fabrication of MgO transparent ceramics using commercial nanocrystalline powders with an average grain size of 52 nm by SPS technology, and the maximum transmittance of as-prepared ceramic is 60 % at 700 nm when sintered at 800 °C and 150 MPa for 5 min. Despite this progress, SPS-fabricated MgO ceramics still require high temperatures (>1500 °C and elevated pressures (150 MPa)), which limits their application [19].

Sintering additives [20–25] play a critical role in further reducing sintering temperatures and improving densification of MgO ceramics. Previous studies have explored various additives, including LiF , Yb_2O_3 and CaO. For instance, Jiang et al. [20] fabricated transparent MgO ceramics by SPS with commercial MgO powders and used LiF as the sintering aid. For the MgO ceramic sintered at 900 °C for 5 min under 30 MPa from powders with 1 wt % LiF, the transmittance was 30 %–40 % at 800 nm. It suggests that a small amount of sintering aid can enhance densification when a low sintering pressure is applied. However, LiF doping undermines the mechanical properties of ceramics, thus limiting their applicability—especially for high-temperature uses. Chen et al. [21] reported the fabrication of Yb-doped MgO transparent ceramics via SPS. Under the optimized sintering conditions (105 MPa, 1100 °C, 60 min), the sample doped with 0.02 % Yb achieved a maximum transmittance of 80 % at 1030 nm. These findings demonstrate that an appropriate amount of homogeneously dispersed Yb_2O_3 contributes to enhanced densification while retarding grain growth. Tran et al. [22] prepared 0.4 mol % Ca-doped MgO ceramics via SPS, 300 MPa, (650–800) °C, (15–30) min. The doped samples achieved >99 % relative density with nanometric grain sizes (29.1–69.3) nm.

Y_2O_3 has been widely used as a sintering aid for oxide ceramics due to its high melting point, large ionic radius and chemical stability. Previous studies have confirmed that Y_2O_3 can induce lattice distortion when dissolved into host lattices (e.g., MgO, Al_2O_3) owing to ionic radius differences, which promotes atomic diffusion and densification. Meanwhile, excess Y_2O_3 tends to form second-phase particles at grain boundaries, inhibiting abnormal grain growth via the Zener pinning effect [26–27]. Simultaneously, Y_2O_3 can improve the morphology, microstructure and comprehensive performance of the ceramics [28]. Zhou et al. [26] reported the preparation of highly dense translucent MgO ceramics via pressureless vacuum sintering, using MgO powder as the raw material and Y_2O_3 as the sintering aid. The results show that the MgO ceramics doped with 1.5 wt % Y_2O_3 achieve a relative density of 98.9 %, a hardness of 8.07 GPa, and a transmittance of 45.9 % at a wavelength of 1400 nm. Zhang et al. [27] prepared high-performance MgO ceramics from fine magnesite via one-step sintering with Y_2O_3 as the sintering aid. Their study on Y_2O_3-doped MgO ceramics by a novel precursor-sintering process showed that 5 wt % Y_2O_3 doping formed a limited Y_2O_3-MgO solid solution, significantly promoting densification and mechanical properties. The enhancement mechanisms were lattice distortion from the Y^{3+}/Mg^{2+} ionic radius difference and reduced dislocation density via synergistic grain boundary migration, laying a theoretical basis for low-cost stable MgO ceramics preparation. However, the underlying mechanisms of Y_2O_3 in SPS-processed transparent MgO ceramics remain unclear. Although existing studies have achieved full densification and improved performance of MgO-Y_2O_3 composite ceramics via SPS at (1200–1400) °C studies on the addition of a small amount of Y_2O_3 are still lacking [29–30].

This work advances existing research by: (1) optimizing the process parameters of the SPS method for preparing transparent MgO ceramics; (2) optimizing the Y_2O_3 content (1.5 wt %) to achieve low-temperature (1350 °C) sintering with higher transmittance (75.35 %) than previous studies; (3) clarifying the mechanism of Y^{3+} ion incorporation into the MgO lattice. The findings offer insights into the low-temperature fabrication of high-transmittance MgO ceramics via Y_2O_3-assisted SPS.

2. Materials and Methods

2.1. Raw Materials and Powder Preparation

High-purity MgO powders (self-synthesized via the electrolysis method) with a nanoflake morphology were used as the starting material. Y_2O_3 powders (99.9 %, Sinopharm Chemical Reagent Co., Ltd., Shanghai,

 https://doi.org/10.64486/m.66.1.4

China) were added as a sintering aid at mass fractions of 0, 0.5 wt %, 1.0 wt %, 1.5 wt %, and 2.0 wt %. For each composition, 100 g of powder mixture was ball-milled in 200 mL of ethanol using a planetary ball mill (F-P4000, Hunan Focucy Experimental Instruments Co., Ltd., Changsha, China) at 400 rpm for 8 h. Zirconia balls (10, 5, and 2 mm in diameter) were used as grinding media, which were mixed together in the same milling run at a weight ratio of 3:3:4 and a total ball-to-powder weight ratio of 5:1. The slurry was dried at 80 °C for 12 h, gently ground, and sieved through a 200-mesh screen to obtain uniformly granulated powders.

2.2. Sample Preparation

The MgO ceramics (pure MgO and Y_2O_3-doped MgO) were fabricated by SPS using an SPS-2T-2-MIN[H] apparatus (Shanghai Chenhua Technology Co., Ltd., Shanghai, China). A uniaxial double-sided pressing graphite die with cylindrical cavity and punches was used for ceramics consolidation. The sintering process was carried out in vacuum at a residual pressure of not more than 10^{-3} Pa, which effectively mitigates gas-induced contamination and facilitates the densification of the ceramic samples. Approximately 1.5 g of powder was loaded into the graphite die with an inner diameter of 15 mm. To prevent reactions and facilitate demolding, 0.2 mm thick graphite foils were placed between the powder and the die surfaces. A uniaxial pressure of 30 MPa was applied at the beginning of the process to ensure proper contact between the spacers and the graphite die during the application of pulsed electric current. The samples were heated using unipolar low-voltage pulsed current in an on/off regime, where the pulse duration was 30 ms (on) and the inter-pulse interval was 4 ms, resulting in a single pulse cycle of 34 ms. The temperature was first raised to 600 °C within 6 min under program control, monitored by a thermocouple positioned near the die wall. Subsequently, the heating rate was set to 25 °C/min to reach the designated sintering temperatures (1400 °C, 1450 °C, 1500 °C, 1550 °C, 1600 °C , for parameter optimization; 1350 °C for Y_2O_3-doped samples). For the Y_2O_3-doped MgO system, pre-experiments were systematically conducted to investigate the effects of sintering temperature (1250–1500) °C and holding time (5–20 min) on the densification and microstructure of the samples. Ultimately, 1350 °C , and 10 min were selected as the optimized base parameters for the doping experiments, which were referenced from relevant research results and verified by experiments to balance densification and grain growth. During the high-temperature stage (≥600 °C) temperature measurement and feedback control were switched to an optical pyrometer (low detection threshold ≥600 °C) focused on a non-through hole (depth ~5 mm) drilled in the upper graphite plunger, ensuring accurate temperature monitoring of the sample region. The samples were held at the target temperature for (5–30) min (depending on experimental groups).

After the isothermal hold, the applied pressure was gradually released at a rate of 10 MPa/min, and the samples were cooled at a controlled rate of 100 °C/min. Upon cooling to 200 °C the chamber was vented to atmospheric pressure, and the samples were allowed to cool naturally to room temperature to avoid thermal shock-induced cracking. The sintered compacts were carefully demolded, and their surface contaminants (residual graphite) were removed by mechanical grinding. Subsequently, the samples were sequentially ground using SiC abrasive papers (400, 800, 1200, 1500, and 2000) grit to achieve a flat surface, followed by fine polishing with 3 μm and 1 μm diamond suspensions (Guangzhou Jinxiang Equipment Inspection Co., Ltd., Guangzhou, China) using a semi-automatic polishing system (Tianjin Ortlai Technology Co., Ltd., Tianjin, China). The final polished specimens were circular with a diameter of 15 mm and a thickness of (1.5 ± 0.1) mm, which was precisely controlled via standardized mechanical grinding and fine polishing procedures to ensure the consistency of sample thickness. This uniform thickness benchmark guarantees the reliability and comparability of optical transmittance measurements for all samples, and the minor thickness deviation is within the acceptable range of experimental error with negligible effect on transmittance results.

2.3. Characterization Methods

X-ray diffraction (XRD) analysis was performed using a D8 Advance diffractometer (Bruker Corporation, Bielefeld, Germany) with a Cu Kα radiation. During the study, a voltage of 40 kV and a current of 30 mA were applied to the anode copper tube (λ = 1.541 Å). The scanning was conducted in the 2θ range of 10°–80° with a step size of 0.02° and a scanning rate of 0.05°/s. To improve signal-to-noise ratio and eliminate weak background

https://doi.org/10.64486/m.66.1.4

interference, mild smoothing and linear background subtraction were applied to the XRD patterns using MDI Jade 6.5 software, without altering the original peak position, relative intensity, or peak width characteristics. No Kα2 stripping was performed. Phase identification was carried out using the processed patterns combined with the international crystallographic database.

The density of the sintered samples was determined via the Archimedes method in deionized water in accordance with the Chinese standard GB/T 25995–2010, with two types of density measurements distinguished based on the actual pore state of the samples. Prior to the measurement, all samples were immersed in ethanol and ultrasonically treated to remove surface air bubbles, then dried completely for testing. The theoretical density of pure MgO was fixed at 3.58 g/cm^3, and the theoretical density of Y_2O_3-doped MgO samples was calculated by the rule of mixtures according to the mass fraction of each component. Each sample was measured three times independently, and the average value was adopted for subsequent analysis. For most sintered samples (excluding the pure MgO sample sintered at 1600 °C), the open pores on the surface were filled with graphite impurities derived from the graphite die and foil during SPS sintering, resulting in the inaccessibility of the open pore structure to the test medium. Thus, only the bulk density ($V_{\text{solid mat.}} + V_{\text{close pores}} + V_{\text{open pores}}$) was measured for these samples. For the pure MgO sample sintered at 1600 °C, the graphite impurities were mostly burned off at the ultra-high temperature, leaving empty open pores in the ceramic matrix. Therefore, the apparent density ($V_{\text{solid mat.}} + V_{\text{close pores}}$) was measured for this specific sample. The relative density was calculated as the ratio of the measured actual density (bulk density for most samples, apparent density for the 1600 °C pure MgO sample) to the corresponding theoretical density.

Fourier transform infrared (FTIR) transmittance measurements were performed using a WQF-510A spectrometer (Beifeng Rayleigh Analytical Instruments Co., Ltd., Beijing, China) in the mid-infrared wavelength range of (2300–10000) nm. The samples were placed in a sample holder with a circular aperture of 5 mm in diameter, and the transmittance was recorded with a resolution of 4 cm^{-1} and 32 scans for signal averaging. Pure air was selected as the reference for background spectrum collection, as it directly captures the "blank" environmental baseline and thereby enables effective elimination of interferences such as atmospheric absorption. All transmittance tests were carried out on samples with the unified thickness of (1.5 ± 0.1) mm, and the transmittance comparison of different samples was based on this thickness benchmark. The slight thickness deviation has no obvious impact on the variation trend of transmittance with sintering parameters and Y_2O_3 doping content, which does not affect the conclusion of this study.

For microstructure observation, the polished samples were thermally etched in a muffle furnace under ambient atmosphere at a temperature 50 °C lower than the corresponding sintering temperature for 30 min to reveal grain boundaries. The microstructures were characterized using a Hitachi SU8100 field emission scanning electron microscope (FE-SEM) (Hitachi, Ltd.,Tokyo, Japan) operated at an accelerating voltage of 15 kV and a working distance of 8 mm. An Oxford Ultim Max40 Energy-dispersive X-ray spectroscopy (EDS) (Oxford Instruments, Oxford, England) was used for map scanning to analyze the elemental distribution of Y_2O_3 in the MgO matrix. Grain size statistics were performed using Nano Measurer 1.2 software: ≥200 grains were randomly selected from SEM micrographs (at ×5000 magnification) to calculate the average grain size via the linear intercept method. Complementary metallographic observations were conducted using an MDS300 metallographic microscope (Beijing Outaiwei Industry Trading Co., Ltd., Beijing, China) to confirm pore distribution and grain uniformity.

3. Results and Discussion

Figure 1 shows the merged XRD pattern and SEM micrograph of MgO powder. The XRD pattern (Figure 1a) exhibits sharp peaks corresponding to cubic MgO (PDF#77-2364). The SEM image (Figure 1b) reveals nanoflake-shaped particles with slight agglomeration, with a multimodal particle size distribution.

https://doi.org/10.64486/m.66.1.4

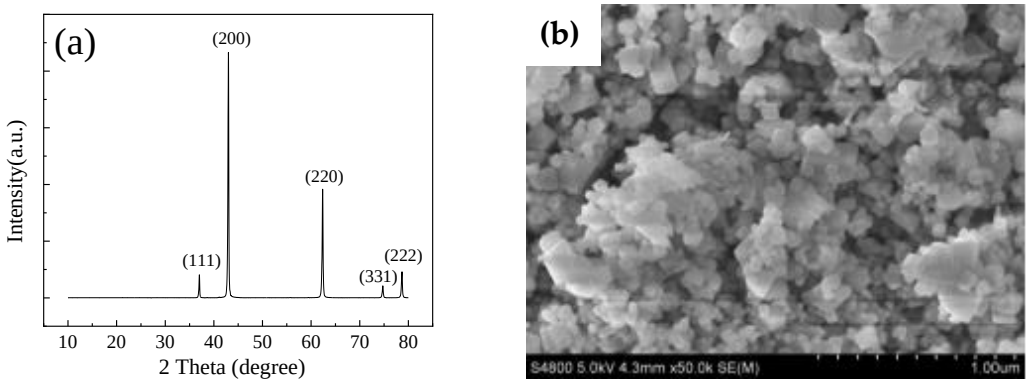

Figure 1. XRD pattern (a) and SEM micrograph (b) of MgO powder

3.1. Effect of Sintering Temperature on the Properties of MgO Ceramics

Figure 2a shows the variation of relative density with temperature for SPS-fabricated samples at a constant holding time of 10 min. Within the temperature range of (1400–1600) °C the relative density of MgO ceramics initially increases and subsequently decreases, reaching a maximum of 98.53 % at 1550 °C. A slight reduction in relative density is observed upon further heating to 1600 °C which is attributed to three key factors: first, excessively high temperatures induce rapid grain growth of MgO grains and a sharp decrease in active grain boundaries (the dominant sites for atomic diffusion during densification), reducing the migration activity of MgO grain boundaries and impeding further densification; second, the elevated MgO vapor pressure at high temperatures causes slight volatilization loss of the matrix, leading to the formation of microvoids and a loose internal structure [31]; third, the graphite impurities filling the open pores are mostly burned off at 1600 °C exposing the empty open pore structure of the ceramic. For this sample, the apparent density was measured instead of the bulk density (adopted for other samples), which also contributes to the slight decrease in the calculated relative density. Overall, the relative density fluctuates between 96.90 % and 98.53 % in the investigated range, markedly exceeding that of conventionally sintered MgO ceramics under comparable conditions [32]. These results demonstrate the pronounced densification efficiency of SPS technology.

Figure 2b presents the transmittance curves of MgO ceramics sintered at various temperatures. Across all conditions, the transmittance exhibits a similar wavelength-dependent trend: it increases sharply in the 2300–6500 nm region, reaches a maximum, and then gradually decreases. Two minor peaks appear at 7600 nm and 8800 nm, followed by a continuous decline until nearly zero at 10000 nm. The maximum transmittance initially rises with increasing sintering temperature and subsequently decreases at excessively high temperatures. At 6500 nm, the transmittance values corresponding to sintering temperatures of 1400 °C, 1450 °C, 1500 °C, 1550 °C, and 1600 °C are 23.68 %, 28.11 %, 40.40 %, 50.34 %, and 47.66 %, respectively. The improvement in transmittance at elevated temperatures is primarily attributed to the reduction of porosity and enhanced densification. However, excessive heating leads to a decrease in the relative density of the ceramics, which in turn results in a reduction of optical transmittance. Several weak absorption peaks at 7600–8800 nm are observed, which can be attributed to the stretching vibrations of carbonate groups formed due to contamination from the graphite die and spacers during SPS [33]. It is noteworthy that the highest transmittance of the pure MgO sintered samples is lower than the theoretical transmittance of MgO single crystals, which may originate from the presence of color centers, residual scattering centers, and trace impurity phases (e.g., residual carbon from graphite die contamination) [20, 33]. A detailed analysis of the theoretical transmittance limit and dominant light scattering mechanisms is presented in Section 3.3 in combination with Y_2O_3-doped samples. Since no post-annealing was performed to eliminate these extrinsic effects, the reported FTIR transmittance reflects the as-SPS state and cannot be treated as the intrinsic optical property of MgO ceramics.

https://doi.org/10.64486/m.66.1.4

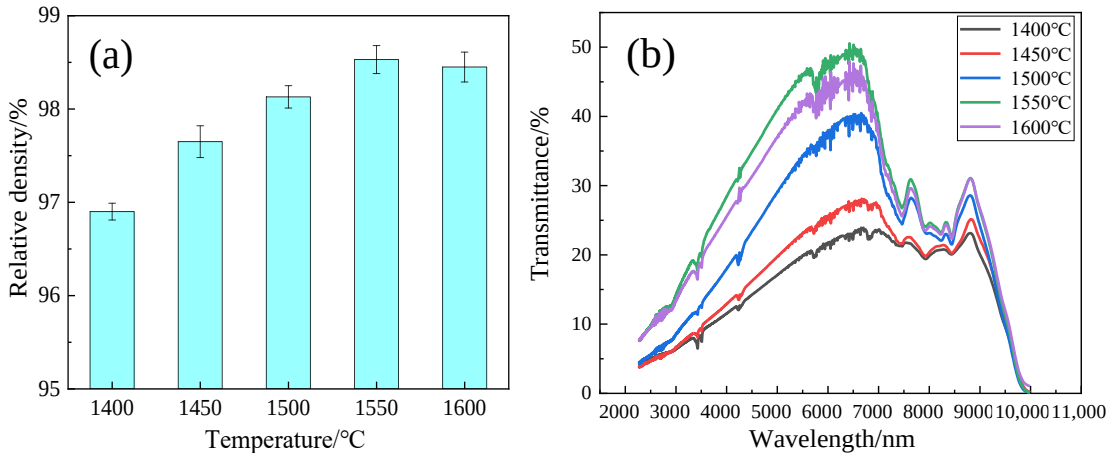

Figure 2. Effect of sintering temperature on relative density (a) and transmittance curves (b) of MgO ceramics

Table 1. Grain sizes of MgO ceramics at different sintering temperatures

Sintering temperature/°C	1400	1450	1500	1550	1600
Grain size/μm	26.48	28.04	29.58	48.13	88.75

The microstructural evolution of MgO ceramics with increasing sintering temperature is illustrated in Figure 3, with the corresponding variation in grain size as a function of sintering temperature summarized in Table 1. Throughout the studied temperature range, the grains undergo normal growth without abnormal coarsening. In the temperature range of 1400–1500 °C the grains grow slowly and moderately with the size remaining relatively stable (26.48–29.58) μm, maintaining a uniform grain size distribution; meanwhile, the black features observed in the micrographs—trace residual carbon impurities (greatly reduced by pre-test thermal etching) and intrinsic micro-pores of the ceramics—are significantly reduced. This slow grain growth with reduced porosity directly contributes to the continuous increase in relative density and optical transmittance observed in this temperature interval, as the reduction of intrinsic micropores (the only factor related to densification) minimizes light scattering and enhances the material's densification level [17]. From 1500 °C to 1600 °C grain growth accelerates with a marked increase in size; in particular, at 1600 °C the grain size is almost twice that at 1550 °C accompanied by a further reduction in the volume fraction of the aforementioned black features. However, at 1600 °C (Figure 3e), despite the overall high density of the ceramics, a small amount of residual black features (mainly intrinsic micropores and trace carbon impurities) is still present. These residual features, lead to a slight decline in relative density and a corresponding reduction in optical transmittance compared with the peak performance at 1550 °C.

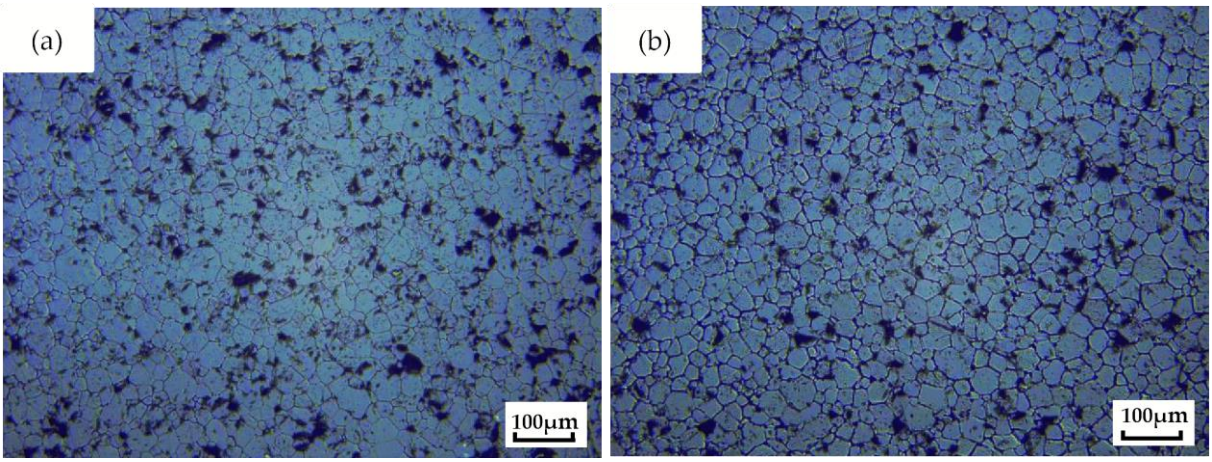

https://doi.org/10.64486/m.66.1.4

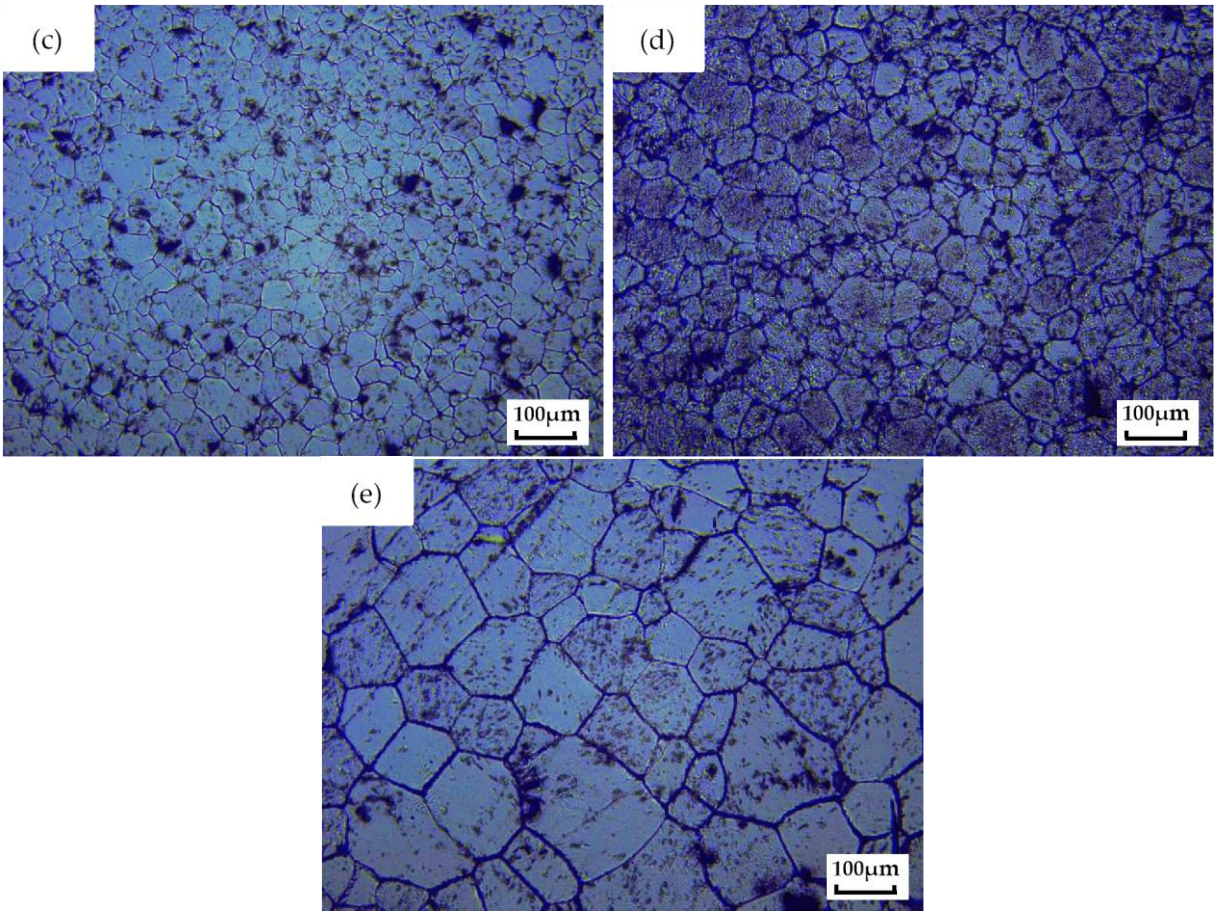

Figure 3. Optical micrographs of MgO ceramics at different sintering temperatures. (a) 1400 °C; (b) 1450 °C; (c) 1500 °C; (d) 1550 °C; (e) 1600 °C

3.2. Effect of Holding Time on the Properties of MgO Ceramics

The sample sintered at 1500 °C was selected for holding time studies because it represents the midpoint of the sintering temperature range, allowing clear observation of densification and grain growth kinetics without excessive volatilization. Figure 4a shows the variation in relative density of SPS-fabricated MgO ceramics with different holding times at a sintering temperature of 1500 °C. It can be seen that the relative density increases from 97.71 % to 98.61 % when the holding time is extended from 5 to 30 min. During the mid-stage of sintering, solid-state diffusion dominates, leading to a rapid densification rate and a marked increase in density [34]. In the later stage, however, the densification rate decreases while grain growth becomes more pronounced. Notably, even at a short holding time of 5 min, the ceramics achieve a relatively high density. Extending the holding time further promotes densification, but the improvement becomes less significant, and the density tends to stabilize.

Figure 4b displays the transmittance curves of MgO ceramics prepared at different holding times. Across all conditions, the transmittance follows a similar wavelength-dependent trend: it increases sharply within the 2300–6500 nm range, reaches a maximum, and then decreases gradually. Several weak absorption peaks are observed at 7600–8800 nm, followed by a continuous decline until nearly zero at 10000 nm. With increasing holding time, the transmittance improves, but beyond 15 min it reaches a plateau, indicating a limited effect of further holding on optical performance. At 6500 nm, the peak transmittance values for holding times of 5, 10, 15, 20, and 30 min are 31.46 %, 40.40 %, 49.89 %, 51.69 %, and 52.21 %, respectively. This trend is consistent with the densification behavior observed in Figure 4a.

https://doi.org/10.64486/m.66.1.4

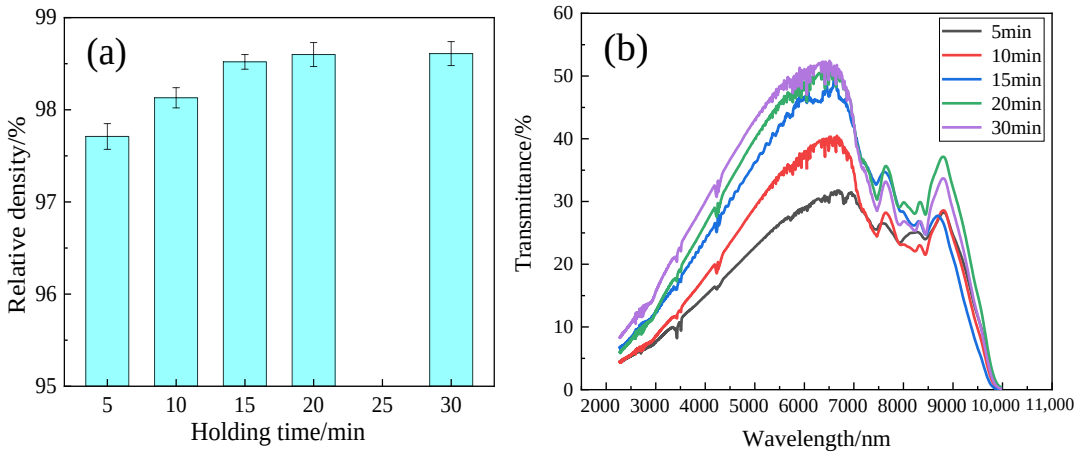

Figure 4. Effect of holding time on relative density (a) and transmittance curves (b) of MgO ceramics

Table 2. Grain sizes of MgO ceramics at different holding times

Holding time/min	5	10	15	20	30
Grain size/μm	20.88	29.58	34.13	45.32	80.68

The microstructural evolution of MgO ceramics with increasing holding time is illustrated in Figure 5, with the corresponding grain size variation summarized in Table 2. Throughout the range of (5–30) min, grains grow uniformly without abnormal coarsening, and the number of black features gradually decreases with longer holding times. When the holding time is below 15 min, grain growth is relatively slow, and the increase in size is limited (20.88–34.13 μm). Beyond 15 min, however, the grain growth rate accelerates markedly with significant coarsening, with the grain size rising sharply from 34.13 μm at 15 min to 45.32 μm at 20 min and further to 80.68 μm at 30 min. Under elevated temperatures and external load, prolonged holding time enhances atomic rearrangement and lattice diffusion, which in turn promote grain boundary contact and surface diffusion. These dynamic processes facilitate the formation and growth of intergranular necks, accompanied by the diffusion of vacancies away from the neck region. As a result, the neck structures continuously expand and connect, and the MgO grains gradually coarsen with increasing holding time.

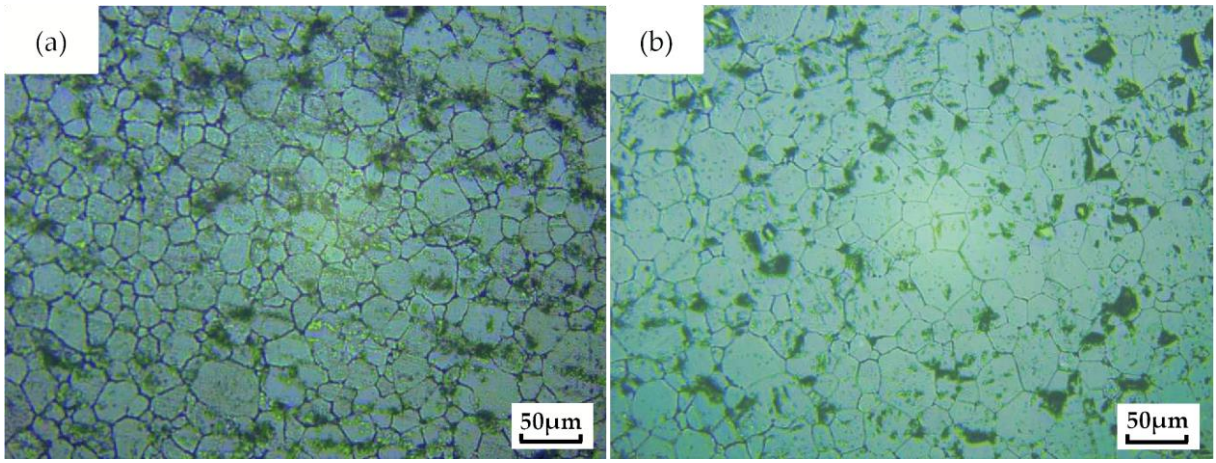

https://doi.org/10.64486/m.66.1.4

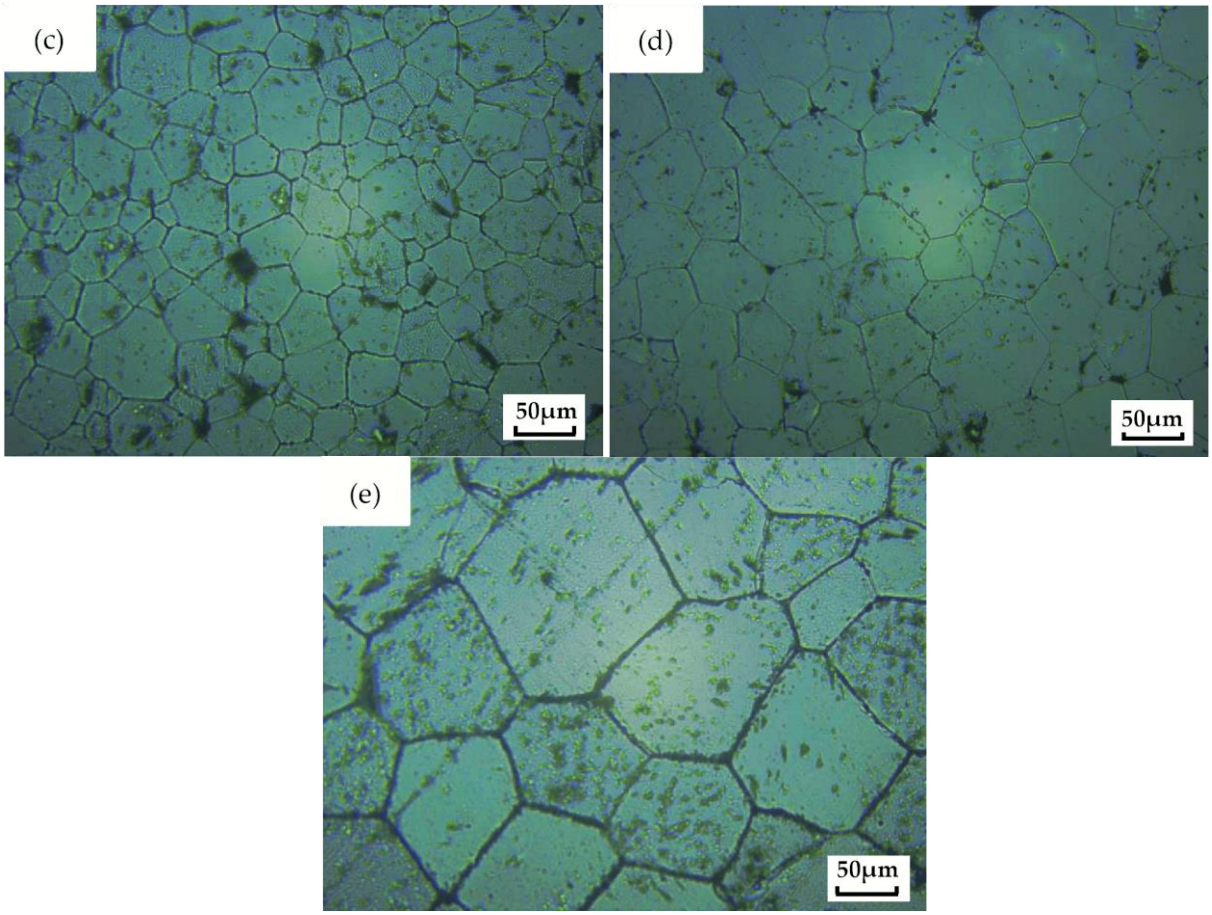

Figure 5. Optical micrographs of MgO ceramics at different holding times. (a) 5 min; (b) 10 min; (c) 15 min; (d) 20 min; (e) 30 min

3.3. Effect of Amount of Y_2O_3 on the Properties of MgO Ceramics

Figure 6a displays the XRD patterns of Y_2O_3-doped MgO ceramics sintered at 1350 °C for a 10 min holding time. All samples exhibit sharp, intense MgO diffraction peaks, indicative of well-developed crystallinity; notably, only the pure MgO phase is detected when the Y_2O_3 content is below 1 wt %. This observation suggests that the solubility limit of yttrium in the MgO lattice likely falls within the range of 0.5–1 wt % under the present SPS conditions. Figure 6b presents a magnified view of the MgO (200) crystal plane, where the corresponding diffraction peaks show a distinct shift trend. The MgO (200) crystal plane was selected for lattice parameter calculation because it is the strongest diffraction peak of cubic MgO with a sharp peak shape and high signal-to-noise ratio, which can effectively reduce the calculation error caused by peak fitting and background interference. Meanwhile, this crystal plane has high sensitivity to lattice distortion induced by Y^{3+} doping, and this selection method has been widely applied in the lattice parameter analysis of rare earth-doped MgO ceramics [21,27]. As the Y_2O_3 content increases from 0 to 1 wt %, the diffraction peaks gradually shift toward lower angles—confirming that Y_2O_3 dissolves into the MgO lattice, inducing lattice distortion (evidenced by the increased lattice constant in Table 3) and lattice activation to facilitate sintering. This phenomenon aligns with the mechanism proposed by Zhang et al. [27], where ionic radius mismatch between dopant and host ions creates lattice defects that act as diffusion channels, promoting atomic migration and densification. When the Y_2O_3 doping level exceeds 1 wt % (1.5 and 2 wt %), the rate of the peak shift toward lower angles slows dramatically. This implies that the solid solubility of Y_2O_3 in MgO approaches saturation, with the excess Y_2O_3 failing to effectively incorporate into the MgO lattice attributed to the considerable ionic radius discrepancy between Y^{3+} (0.89 Å) and Mg^{2+} (0.72 Å). The calculated lattice constants (summarized in Table 3) further verify this: the lattice constant increases with rising Y_2O_3 content, confirming the incorporation of dissolved Y_2O_3 into the MgO matrix

https://doi.org/10.64486/m.66.1.4

[27]; however, the increment of lattice constant slows down significantly when the Y_2O_3 doping level reaches 1 wt %, providing additional support that the solubility limit of Y_2O_3 in MgO is nearly reached under the investigated SPS conditions, and excess Y_2O_3 can only be partially dissolved.

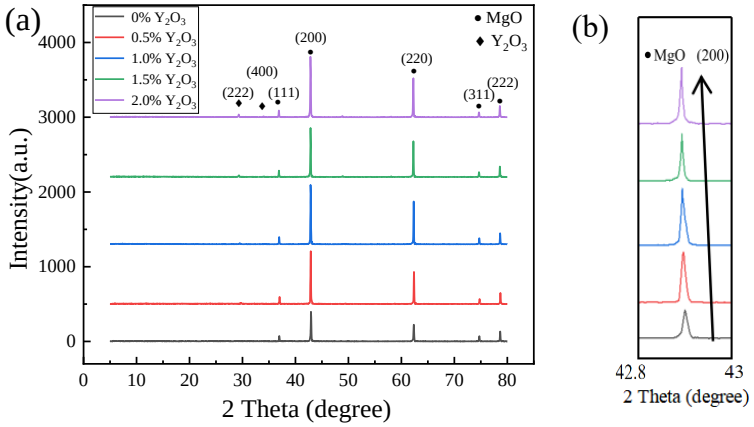

Figure 6. XRD patterns of MgO ceramics with different Y_2O_3 contents: (a) Y_2O_3-doped MgO ceramics; (b) magnified image of MgO (200) crystal plane

Table 3. Lattice parameters (Å) of MgO (200) crystal plane and Y_2O_3 (222) crystal plane

Compositions	Pure MgO	0.5 wt % Y_2O_3-doped MgO	1 wt % Y_2O_3-doped MgO	1.5 wt % Y_2O_3-doped MgO	2 wt % Y_2O_3-doped MgO
MgO (200)/Å	4.2108	4.2126	4.2145	4.2154	4.2158
Y_2O_3 (222)/Å	—	—	10.5393	10.5364	10.5352

Figure 7a shows the relative density of SPS-fabricated MgO ceramics with different Y_2O_3 contents. Compared with pure MgO (96.03 %), the relative density increases significantly upon Y_2O_3 addition, reaching a maximum of 99.02 % at 1.5 wt %. This demonstrates that although the solid solubility limit of Y_2O_3 is reached at a content of 1 wt %, the small amount of impurity phase formed in the samples when the Y_2O_3 content exceeds 1 wt % can still improve the bulk density of MgO ceramics to a certain extent and thus facilitate densification. However, when the Y_2O_3 content increases to 2 wt %, the relative density slightly decreases to 98.99 %. This may be attributed to the fact that excessive impurity phases reduce the direct contact between MgO particles, interfere with the mass transfer process, and thus reduce the sintering degree [35].

Figure 7b shows the transmittance curves of MgO ceramics as a function of Y_2O_3 content. The transmittance first increases and then slightly decreases with increasing Y_2O_3, exhibiting a trend consistent with the relative density. Pure MgO ceramics display poor transparency, with a maximum transmittance of only 17.76 % at 6700 nm. In contrast, Y_2O_3 doping significantly improves transmittance. When the Y_2O_3 content is 1.5 wt %, the MgO ceramic samples achieve the highest transmittance, reaching 75.35 % at a wavelength of 5500 nm.

To further evaluate the optical quality of the prepared ceramics, the experimental transmittance is compared with the theoretical transmittance limit of a fully dense, defect-free MgO single crystal. For such a single crystal, the theoretical in-line transmittance, which is only limited by Fresnel reflection can be calculated as approximately 87 % using the formula $T = 2n / (n^2 + 1)$ [33]. In this work, the maximum measured transmittance (75.35 %) is about 12 % lower than this single-crystal limit, a difference primarily attributed to light scattering within the polycrystalline ceramic.

The main scattering sources in this study are residual pores and grain boundary-related scattering. On the one hand, with increasing Y_2O_3 addition, the relative density of MgO ceramics increases continuously while porosity decreases gradually. Owing to the significant refractive index mismatch between pores ($n \approx 1$) and the MgO matrix ($n \approx 1.7$) [36], residual pores act as strong light-scattering centers; this is the main reason for the

https://doi.org/10.64486/m.66.1.4

gradual transmittance increase at Y_2O_3 contents below 1.5 wt %. On the other hand, the slight transmittance decrease in the 2.0 wt % Y_2O_3-doped sample is attributed to two factors: (1) the formation of Y-rich secondary phases at grain boundaries (confirmed by XRD and EDS characterizations in Figures 6 and 9), which introduce additional scattering centers due to refractive index mismatch with the MgO matrix [17]; and (2) enhanced light refraction induced by these impurity phases, which further degrades the overall optical transparency [30]. Collectively, these scattering mechanisms, in combination with the microstructural features (Figure 8), govern the optical transmittance of Y_2O_3-doped MgO ceramics.

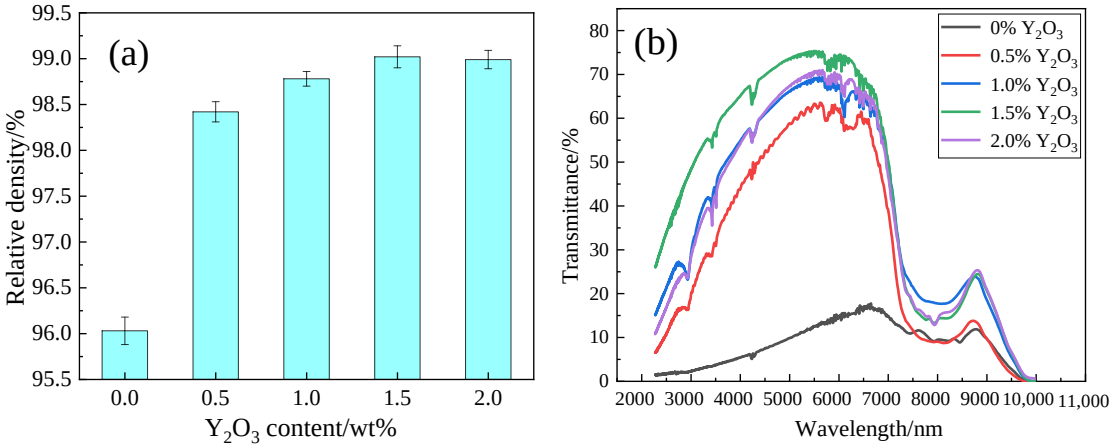

Figure 7. Effect of Y_2O_3 content on relative density (a) and transmittance curves; (b) of MgO Ceramics

Table 4. Grain sizes of MgO ceramics with different Y_2O_3 contents

Y_2O_3 content/wt %	0	0.5	1	1.5	2
Grain size /μm	13.75	7.13	5.96	4.53	3.85

Figure 8 shows the microstructures of MgO ceramics with different Y_2O_3 contents, including optical micrographs (8a–e) for overall grain morphology observation and SEM micrographs (8f, 8g) for clear identification of pores that are difficult to distinguish in optical micrographs. As presented in Table 4, the grain size of MgO ceramics exhibits a significant decreasing trend with the increase in Y_2O_3 content. For the pure MgO sample (0 wt % Y_2O_3), normal grain growth is observed with a relatively uniform size (13.75 μm), yet numerous pores and defects are present (Figure 8f), which is clearly visualized by the SEM micrograph. With the addition of Y_2O_3, the grain uniformity is improved and the porosity is markedly reduced (Figure 8g); the grain size decreases from 13.75 μm (0 wt %) to 3.85 μm (2 wt %), and basically stabilizes when the Y_2O_3 addition exceeds 1 wt % . When the Y_2O_3 content is 2 wt %, the grains are tightly packed with negligible pores, as confirmed by both optical and SEM micrographs.

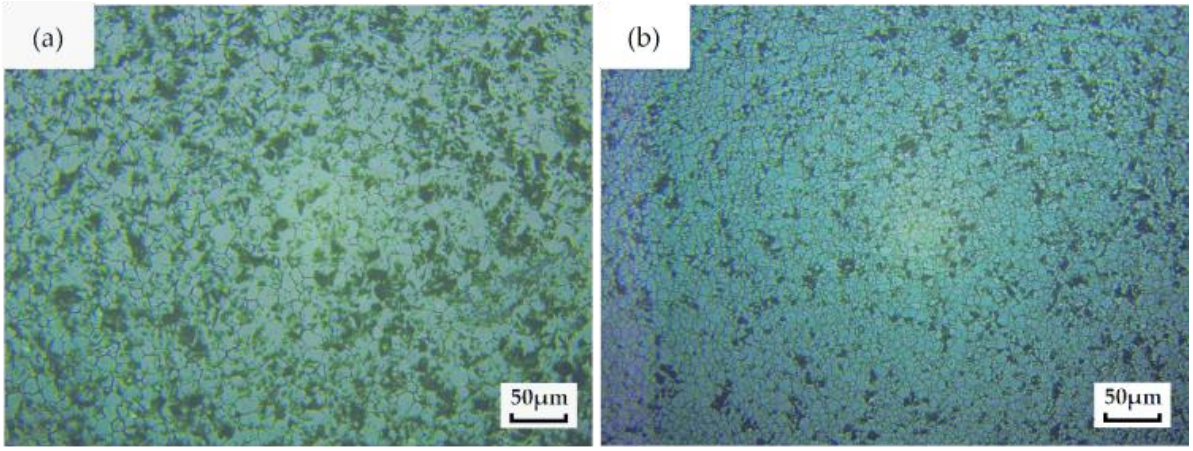

https://doi.org/10.64486/m.66.1.4

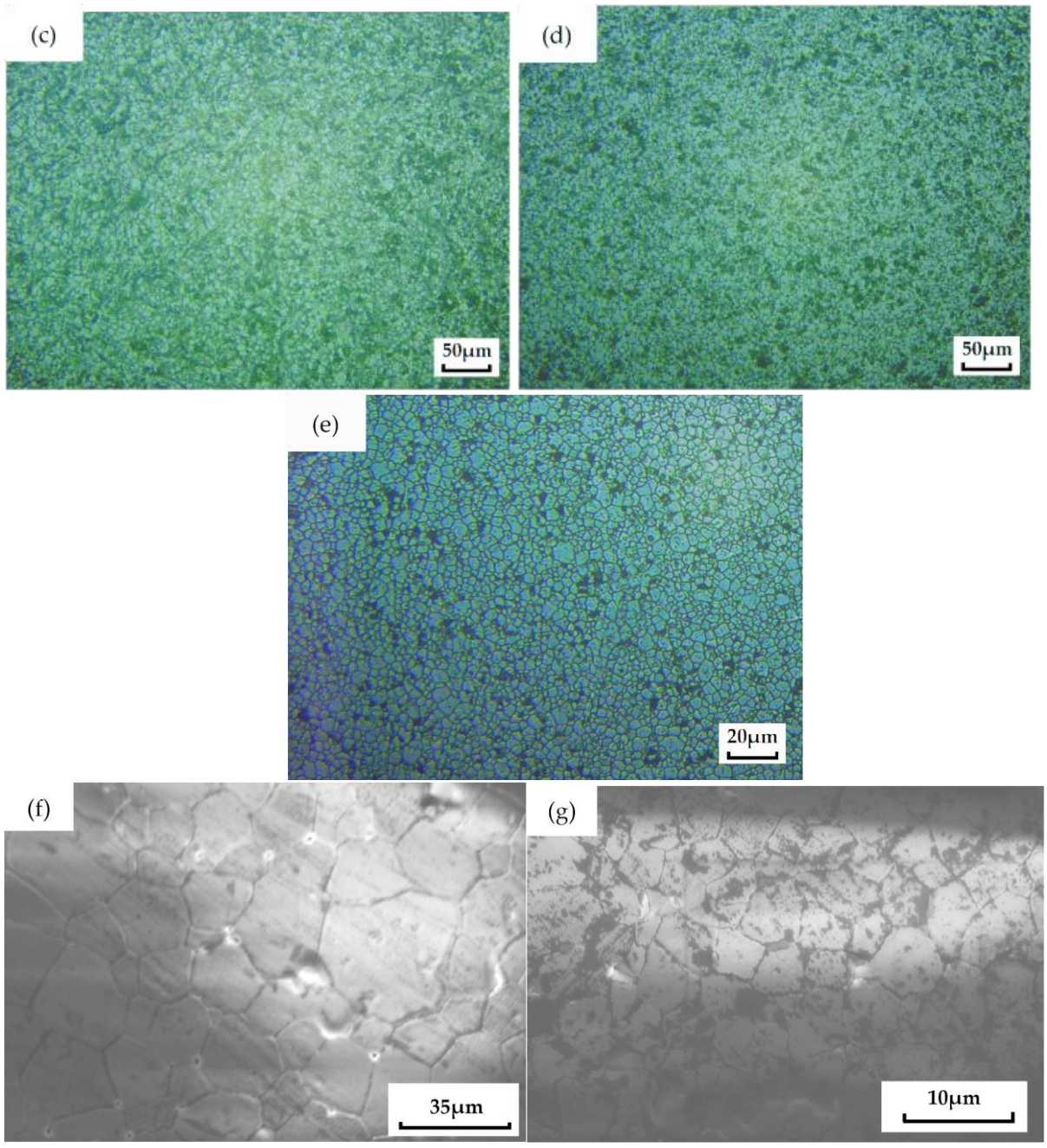

Figure 8. Micrographs of MgO ceramics with different Y_2O_3 contents. (a), (f) 0 wt %; (b) 0.5 wt %; (c) 1 wt %; (d) 1.5 wt %; (e), (g) 2 wt %

Figure 9 presents the EDS mapping results of the 2 wt % Y_2O_3-doped MgO ceramic sample. The results confirm that yttrium is uniformly distributed in the ceramic matrix; meanwhile, excess Y elements (beyond the solubility limit of Y_2O_3 in MgO) exhibit obvious enrichment at grain boundaries. For C element, it shows an overall uniform distribution in the ceramic matrix, while localized C enrichment is observed at the black regions in the SEM micrographs, indicating that the black areas in SEM images correspond to C-enriched zones. Owing to the different imaging principles of optical and electron microscopes, the black spots observed in the optical micrographs (8a–e) are attributed to the combined effects of C element enrichment and residual micro-pores in the ceramics.

The grain boundary segregation of Y elements exerts a typical Zener pinning effect [21,26], which effectively restricts grain boundary migration and inhibits abnormal grain growth of MgO. This mechanism is con-

https://doi.org/10.64486/m.66.1.4

sistent with the observed microstructural evolution, including the significant grain size reduction and remarkable porosity decrease in the samples with increasing Y_2O_3 doping. Similar grain refinement effects via Y_2O_3-induced grain boundary pinning in Y_2O_3-MgO ceramics have also been reported by Wang et al. [30], which further supports the above mechanism.

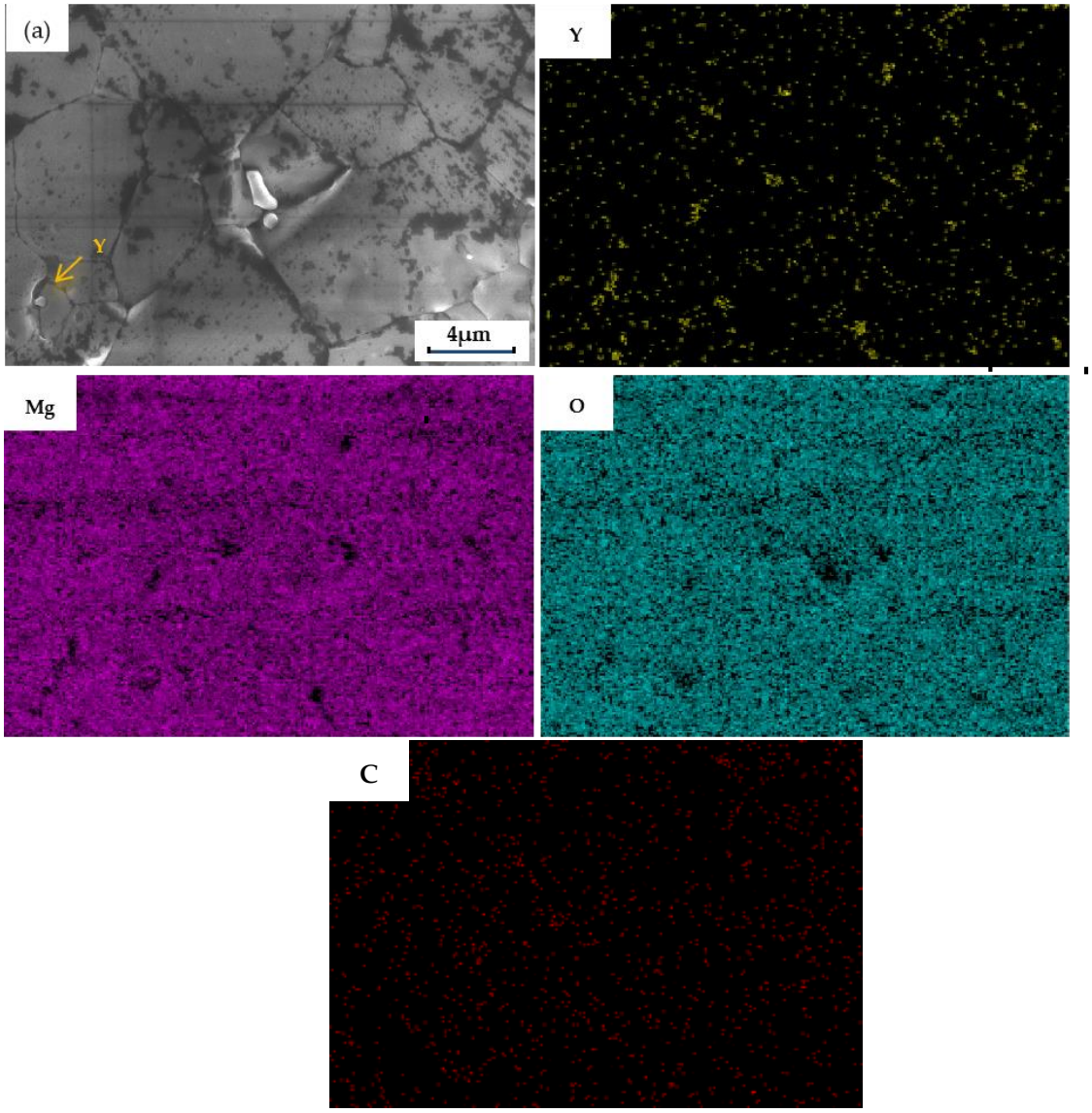

Figure 9. Microstructure and elemental distribution of the MgO ceramic with 2 wt % Y_2O_3: (a) SEM image of the sample; elemental maps of (b) Y, (c) Mg, (d) O, and (e) C

3.4. Summary of Present and Reported Results

Table 5 summarizes the key SPS sintering parameters and corresponding properties of transparent MgO ceramics in this work and previous literatures. Due to the differences in experimental conditions (e.g., sample thickness, testing wavelength window) among various studies, direct performance comparison is not conducted herein. This table aims to provide a contextual reference for the research progress in the field, highlighting the characteristics of the present work under specific SPS conditions.

Notably, under the moderate SPS conditions of 1350 °C, 30 MPa for 10 min, the MgO ceramics doped with 1.5 wt % Y_2O_3 in this work achieve a high relative density of 99.02 % and a maximum mid-infrared transmittance of 75.35 %. Compared with the previously reported literatures (Ref. [17, 18, 19, 21]), this work demonstrates superior sintering efficiency at a relatively lower temperature and pressure, while maintaining excellent optical

 https://doi.org/10.64486/m.66.1.4

transparency. Specifically, Ref. [17] required a higher pressure (70 MPa) and similar temperature (1250 °C) to obtain 85 % transmittance, whereas our work achieves a high mid-infrared transmittance under milder SPS conditions compared with Ref. [17], considering the differences in sample thickness and test wavelength. Moreover, unlike Ref. [21] which focuses on near-infrared transparency, the present work achieves high transmittance in the technologically important mid-infrared region (5.5 μm). These results confirm the technical advantages and novelty of the proposed low-temperature SPS route with Y_2O_3 doping for fabricating high-performance MgO transparent ceramics.

Table 5. Comparison of sintering and infrared optical properties of transparent MgO ceramics

Research Source	Sintering Process SPS	Relative Density/%	Sample Thickness mm	Testing Wavelength Window	Maximum Transmittance/%	Grain Size	Notes
This work	T = (1350–1600) °C t = (5–30) min P = 30 MPa	96.03–99.02	1.5	5.5 μm (Mid-IR)	75.35	(3.85–88.75) μm	Y_2O_3 added as sintering aid; no post-treatment applied, focusing on the direct effects of SPS process
Ref. [17]	T = 1250 °C t = 60 min P = 70 MPa	≥98	2	(2–6) μm (Mid-IR)	85	(3–8) μm	LiF used as a sintering agent, which acts as a physical buffer to reduce carbon penetration
Ref. [18]	T = (700–800) °C t = 5 min P = (100–150) MPa	91–100	1.5	700 nm (Visible)	60	(30–63) nm	No post-treatment applied, focusing on the direct effects of SPS process
Ref. [19]	T = (900–1420) °C t = (3–8) min P = 30 MPa	91.1–95.2	--	--	--	(0.29–4.2) μm	No post-treatment applied, focusing on grain growth behavior during SPS process
Ref. [21]	T = 1100 °C t = (5–60) min P = 105 MPa	≥99.20	1.5	1030 nm (Near-IR)	80	(4.58–12.52) μm	Yb_2O_3 added as a sintering aid, which promotes densification and retards grain growth

Footnote: All data are reproduced as reported in the original literatures. Due to variations in sintering conditions, sample thickness, and testing wavelength window, direct performance comparison is not feasible. This table is intended to provide contextual reference for research progress in the field.

https://doi.org/10.64486/m.66.1.4

4. Conclusions

This work systematically explores the fabrication of MgO transparent ceramics via SPS technology, focusing on process optimization and the modulatory role of Y_2O_3 as a sintering aid, with the following key conclusions:

(1) Sintering temperature and holding time significantly affect the densification and optical performance of pure MgO ceramics. The relative density and transmittance first increase and then decrease with increasing sintering temperature (1400–1600) °C, reaching a peak at 1550 °C. Extending the holding time (5–30) min at 1500 °C promotes densification, but the improvement in transmittance plateaus after 15 min, indicating that moderate sintering parameters balance densification and grain growth.

(2) Y_2O_3 doping effectively reduces the sintering temperature and enhances the comprehensive performance of MgO ceramics. The optimal Y_2O_3 content is 1.5 wt %, which enables sintering at 1350 °C (a 200 °C reduction compared with the optimal sintering temperature of undoped MgO ceramics) while achieving a maximum transmittance of 75.35 % in the mid-IR range. This is attributed to the synergistic effects of lattice distortion induced by Y^{3+}/Mg^{2+} ionic radius differences (evidenced by XRD lattice parameter variations) and grain boundary pinning by excess Y_2O_3 (verified via SEM-EDS characterization), which jointly promote densification and inhibit grain coarsening. These effects are consistent with the established sintering enhancement mechanisms for rare earth oxide-doped oxide ceramics [21,26, 27].

(3) Under the present SPS sintering conditions (1350 °C, 10 min, 30 MPa), the solubility limit of Y_2O_3 in the MgO matrix is inferred to be approximately 0.5–1 wt %. Below this range, Y_2O_3 forms a solid solution with MgO; above 1 wt %, a small amount of impurity phase is generated and Y elements segregate at grain boundaries, which refines the microstructure and reduces porosity.

(4) This study clarifies the mechanism of Y_2O_3-assisted low-temperature sintering of MgO transparent ceramics and optimizes the SPS process parameters. The proposed method provides a low-cost, efficient route for preparing high-transmittance MgO ceramics, which is of great significance for advancing their practical application in IR windows and other optical components. Future work will focus on further reducing residual defects and improving the mechanical stability of the ceramics for extreme service environments.

Acknowledgments: This work has been supported by the Foundation of Liaoning Provincial Key Laboratory of Energy Storage and Utilization (CNNK202319); "Yingkou Talent Program" Youth Top-Tier Talent Project(YKYCQB202508); Liaoning Provincial Department of Education Project (JYTMS20230062); and the 2023 Liaoning Provincial Joint Fund Project Doctoral Scientific Research Initiation Project (2023-BSBA-308).

References

[1] Q. Li, J. Wang, J. Ma, et al., "Fabrication of High-Efficiency Yb:Y_2O_3 Laser Ceramics without Photodarkening," *Journal of the American Ceramic Society*, vol. 105, pp. 3375–3381, 2022, https://doi.org/10.1111/jace.18305

[2] V. Necina, W. Pabst, "Transparent $MgAl_2O_4$ Spinel Ceramics Prepared via Sinter-Forging," *Journal of the European Ceramic Society*, vol. 41, pp. 4313–4318, 2021, https://doi.org/10.1016/j.jeurceramsoc.2021.02.017

[3] R. P. Yavetskiy, A. E. Balabanov, S. V. Parkhomenko, et al., "Effect of Starting Materials and Sintering Temperature on Microstructure and Optical Properties of Y_2O_3:Yb^{3+} 5at % Transparent Ceramics," *Journal of Advanced Ceramics*, vol. 10, pp. 49–61, 2021, https://doi.org/10.1007/s40145-020-0416-3

[4] Z. Liu, A. Ikesue, J. Li, "Research Progress and Prospects of Rare-Earth Doped Sesquioxide Laser Ceramics," *Journal of the European Ceramic Society*, vol. 41, pp. 3895–3910, 2021, https://doi.org/10.1016/j.jeurceramsoc.2021.02.026

[5] K. Hoggas, S. Benaissa, A. Cherouana, et al., "Mechanical Behavior of Transparent Spinel Fabricated by Spark Plasma Sintering," *Ceramics*, vol. 6, pp. 1191–1209, 2023, https://doi.org/10.3390/ceramics6020072

[6] D. Zhambakin, A. Zhilkashinova, M. Abilev, et al., "Structure and Properties of Spark Plasma Sintered SiC Ceramics with Oxide Additives," *Crystals*, vol. 13, Art. no. 1103, 2023, https://doi.org/10.3390/cryst13071103

[7] X. T. Chen, J. H. Hu, G. A. Chen, et al., "Fabrication of Highly Transparent Y_2O_3-MgO Nanocomposite Ceramics in the Visible-Near-IR Wavelength," *Journal of the European Ceramic Society*, vol. 45, Art. no. 117196, 2025, https://doi.org/10.1016/j.jeurceramsoc.2025.117196

[8] Q. Li, Y. Wang, J. Wang, et al., "High Transparency Pr:Y_2O_3 Ceramics: A Promising Gain Medium for Red Emission Solid-State Lasers," *Journal of Advanced Ceramics*, vol. 11, pp. 874–881, 2022, https://doi.org/10.1007/s40145-022-0579-1

[9] Y. Wei, S. Gu, H. Fang, et al., "Properties of MgO Transparent Ceramics Prepared at Low Temperature Using High Sintering Activity MgO Powders," *Journal of the American Ceramic Society*, vol. 103, pp. 5382–5391, 2020, https://doi.org/10.1111/jace.17267

[10] S. Köbel, D. Schneider, L. J. Gauckler, "Processing of Dense MgO Substrates for High-Temperature Superconductors," *International Journal of Materials Research*, vol. 94, no. 3, pp. 200–207, 2003, https://doi.org/10.3139/146.030200

[11] B. F. Zhao, X. Q. Chen, N. C. Chen, et al., "Low-Temperature-Sintered MgO-Based Microwave Dielectric Ceramics with Ultralow Loss and High Thermal Conductivity," *Journal of the American Ceramic Society*, vol. 106, pp. 1159–1169, 2023, https://doi.org/10.1111/jace.18835

[12] N. Heidari, F. Davar, A. Alhaji, "In Situ Formation of Transparent Spinel with the Spark Plasma Sintering of Magnesia-Alumina Nanocomposite Granules without the Help of Sintering Aid," *Ceramics International*, vol. 48, pp. 1633–1641, 2022, https://doi.org/10.1016/j.ceramint.2021.09.242

[13] L. Liang, "Study on Properties of Mg-Al Spinel Ceramics Prepared by Casting Sintering Method," *Integrated Ferroelectrics*, vol. 217, pp. 27–40, 2021, https://doi.org/10.1080/10584587.2021.1911250

[14] X. Y. Huang, Y. M. Liu, Y. Liu, et al., "Fabrication and Characterizations of Yb:YAG Transparent Ceramics Using Alcohol-Water Co-precipitation Method," *Journal of Inorganic Materials*, vol. 36, pp. 217–224, 2021, https://doi.org/10.1554/jim20200231

[15] E. Papynov, O. Shichalin, V. Apanasevich, et al., "Al_2O_3-Phosphate Bioceramic Fabrication via Spark Plasma Sintering-Reactive Synthesis: In Vivo and Microbiological Investigation," *Journal of Composite Science*, vol. 7, Art. no. 409, 2023, https://doi.org/10.3390/jcs7100409

[16] Z. Fu, X. Li, M. Zhang, et al., "Achieving Fabrication of Highly Transparent Y_2O_3 Ceramics via Air Pre-Sintering by Deionization Treatment of Suspension," *Journal of the American Ceramic Society*, vol. 104, pp. 2689–2701, 2021, https://doi.org/10.1111/jace.17638

[17] M. Sakajio, V. Beilin, M. Mann-Lahav, et al., "Highly Transparent Polycrystalline MgO via Spark Plasma Sintering," *ACS Applied Materials & Interfaces*, vol. 14, 2022, https://doi.org/10.1021/acsami.2c11775

[18] R. Chaim, Z. J. Shen, M. Nygren, "Transparent Nanocrystalline MgO by Rapid and Low-Temperature Spark Plasma Sintering," *Journal of Materials Research*, vol. 19, pp. 2527–2531, 2004, https://doi.org/10.1557/JMR.2004.0334

[19] Y. F. Zhang, A. J. Song, D. Q. Ma, et al., "Sintering Characteristics and Grain Growth Behavior of MgO Nanopowders by Spark Plasma Sintering," *Journal of Alloys and Compounds*, vol. 608, pp. 304–310, 2014, https://doi.org/10.1016/j.jallcom.2014.04.148

[20] N. Jiang, R. Xie, Q. Liu, et al., "Fabrication of Sub-micrometer MgO Transparent Ceramics by Spark Plasma Sintering," *Journal of the European Ceramic Society*, vol. 37, pp. 4947–4953, 2017, https://doi.org/10.1016/j.jeurceramsoc.2017.06.021

[21] X. Chen, G. Zhang, R. Tomala, et al., "Yb Doped MgO Transparent Ceramics Generated Through the SPS Method," *Journal of the European Ceramic Society*, vol. 42, pp. 4320–4327, 2022, https://doi.org/10.1016/j.jeurceramsoc.2022.04.025

[22] T. B. Tran, S. Hayun, A. Navrotsky, et al., "Transparent Nanocrystalline Pure and Ca-Doped MgO by Spark Plasma Sintering of Anhydrous Nanoparticles," *Journal of the American Ceramic Society*, vol. 95, 2012, https://doi.org/10.1111/j.1551-2916.2012.05103.x

[23] D. Valiev, S. Stepanov, V. Paygin, et al., "Structural and Luminescent Peculiarities of Spark Plasma Sintered Transparent $MgAl_2O_4$ Spinel Ceramics Doped with Cerium Ions," *Inorganics*, vol. 10, Art. no. 153, 2022, https://doi.org/10.3390/inorganics10100153

[24] Z. M. Yin, B. H. Zhang, X. J. Mao, et al., "Effect of Volume Ratio on the Performance of Mid-wave Infrared Transparent Gd_2O_3-MgO Composite Ceramics," *Ceramics International*, vol. 49, pp. 14607–14614, 2023, https://doi.org/10.1016/j.ceramint.2023.01.051

[25] J. Li, Y. Q. Wu, "Spark Plasma Sintering of cBN-Y_2O_3 Composite Ceramics," *Ceramics International*, vol. 51, pp. 57115–57125, 2025, https://doi.org/10.1016/j.ceramint.2025.09.424

[26] J. F. Zhou, G. M. Liu, J. G. Yu, "Study of the Y_2O_3 Influence on Properties of Sintering Translucent MgO Ceramics," *Journal of Materials Science and Engineering*, vol. 37, pp. 731–735, 2019, https://doi.org/10.14136/j.cnki.issn1673-2812.2019.05.008

[27] R. Zhang, Z. Liu, L. Yuan, et al., "Synergistic Effects of Lattice Distortion and Grain Boundary Migration on Densification and Mechanical Properties in Y_2O_3-doped MgO-based Ceramics," *Ceramics International*, vol. 52, pp. 1392-1403, 2026, https://doi.org/10.1016/j.ceramint.2025.10.147

[28] L. Wang, S. Wang, P. Xing, et al., "High-performance B_4C-YB_4 Composites Fabricated with Y_2O_3 Additive via Hot-pressing Sintering," *Ceramics International*, vol. 48, pp. 15647–15656, 2022, https://doi.org/10.1016/j.ceramint.2022.02.099

[29] X. Wang, D. Xing, Y. Wang, et al., "Optimizing Sintering Conditions for Y_2O_3 Ceramics: A Study of Atmosphere-Dependent Microstructural Evolution and Optical Performance," *Ceramics*, vol. 8, Art. no. 66, 2025, https://doi.org/10.3390/ceramics8020066

[30] H. T. Wang, X. Liu, X. Gu, et al., "High Infrared Transmittance Y_2O_3-MgO Ceramics Prepared by Spark Plasma Sintering," *Ceramics International*, vol. 51, pp. 53139–53153, 2025, https://doi.org/10.1016/j.ceramint.2025.09.066

[31] Y. Xie, Z. Chen, Y. L. Wu, et al., "Activated Sintering of Activated Carbon-doped Magnesia," *Ceramics International*, vol. 40, pp. 16543–16547, 2014, https://doi.org/10.1016/j.ceramint.2014.08.008

[32] K. Itatani, T. Tsujimoto, A. Kishimoto, "Thermal and Optical Properties of Transparent Magnesium Oxide Ceramics Fabricated by Post Hot-Isostatic Pressing," *Journal of the European Ceramic Society*, vol. 26, pp. 639–645, 2005, https://doi.org/10.1016/j.jeurceramsoc.2005.06.011

[33] D. T. Jiang, A. K. Mukherjee, "Synthesis of Y_2O_3-MgO Nanopowder and Infrared Transmission of the Sintered Nanocomposite," *Nanophotonic Materials*, vol. 7030, Art. no. 703007, 2008, https://doi.org/10.1117/12.795472

[34] S. L. Li, C. J. Song, X. Y. Qin, et al., "Densification and Grain Growth Behavior of Highly Dense MgO Ceramics in Pressureless Sintering," *Ceramics International*, vol. 41, pp. 10148–10151, 2015, https://doi.org/10.1016/j.ceramint.2015.04.115

[35] Q. Z. Huang, G. M. Lu, J. G. Yu, "Sintering and Performance of MgO from Bischofite with ZrO_2 Additive," *Applied Mechanics and Materials*, vol. 455, pp. 11–17, 2013, https://doi.org/10.4028/www.scientific.net/AMM.455.11

[36] S. Cunsolo, P. Dore, C. P. Varsamis, "Complex refractive index of MgO in the far infrared from transmission and reflection measurements," *Infrared Physics*, vol. 33, pp. 539–548, 1992, https://doi.org/10.1016/0020-0891(92)90070-a